Supplementary Material belonging to the paper:

Ir^{II}(ethene): Metal or Carbon Radical?

Authors:

Dennis G. H. Hetterscheid, [†] *Jasper Kaiser,* [†] *Eduard Reijerse,* [‡] *Theo P. J. Peters,* [†] *Simone Thewissen,* [†] *Arno N. J. Blok,* [†] *Jan M. M. Smits,* [†] *René de Gelder* [†] *and Bas de Bruin* [*,†]

[†] Radboud University Nijmegen, Institute for Molecules and Materials, Department of Metal-Organic Chemistry, Toernooiveld 1, NL-6525 ED Nijmegen (The Netherlands),

*e-mail: B.deBruin@science.ru.nl

[‡] Max-Planck-Institut für Bioanorganische Chemie, Stiftstrasse 34-36, D-45470 Mülheim an der Ruhr (Germany).

Additional information about the EPR spectrum of 1^{2+}

In a previous communication[1] we already discussed the EPR spectrum as shown in Figure 1 (see main text). At the time of writing, we did not understand the 5-line (super)hyperfine-coupling pattern of the g_1 signal. Initially it occurred to us that the seemingly 1:4:6:4:1 five-line pattern of the g_1 signal might be caused by superhyperfine coupling with nitrogen and/or hydrogen nuclei. However, simulations assuming coupling with two (nearly) equivalent N-nuclei or coupling with one N-nucleus and two (nearly) equivalent H-nuclei, resulted in a poor fit of the experimental spectrum. A reasonable, but still not very satisfactory simulation was obtained by assuming superhyperfine coupling with four (nearly) equivalent $I=1/2$ nuclei. However, the thus obtained superhyperfine coupling-constant $A_1^H \approx 53 \times 10^{-4} \text{cm}^{-1}$ is

far too large for hydrogen. Nonetheless, to check the possibility of such unusually large hydrogen superhyperfine interactions, we prepared two partially deuterated versions of $\mathbf{1}^{2+}$; namely D_4-$\mathbf{1}^{2+}$ in which the ethene ligand has been replaced by $CD_2=CD_2$ and D_{15}-$\mathbf{1}^{2+}$ in which all Py-*Me* protons and N-*CH₂*-Py methylene protons have been replaced by deuterium. The X-band EPR spectra of these deuterated complexes, both in CD_3OD/D_6-acetone and in MeOH/acetone, were identical to the spectrum of $\mathbf{1}^{2+}$ shown in Figure 2. This definitively excludes the possibility of large hydrogen superhyperfine interactions, because the only remaining hydrogen atoms are located at the pyridine rings, far from iridium. Clearly, another interaction must be responsible for the observed pattern at g_1. To gain more understanding of the g_1 part of the spectrum, we calculated the EPR parameters of $\mathbf{1}^{2+}$ using the ADF package, based on the atom-coordinates from the X-ray structure of $\mathbf{1}^{2+}$. EPR parameters calculated from atom-coordinates of the DFT optimized geometry of $\mathbf{1}^{2+}$ proved nearly identical. The agreement between the experimental ($g_3= 1.975$, $g_2= 2.265$ and $g_1= 2.540$) and calculated g-values ($g_3= 1.930$, $g_2= 2.157$ and $g_1= 2.526$) is remarkable, considering the presence of the heavy iridium centre, which usually degrades the accuracy of DFT property calculations. Also, the calculated iridium and N_{amine} hyperfine interactions ($A_3^{Ir} = 53 \times 10^{-4} \, cm^{-1}$, $A_3^{N} = 18 \times 10^{-4} \, cm^{-1}$) represent the experimental data ($A_3^{Ir} = 46 \times 10^{-4} \, cm^{-1}$, $A_3^{N} = 17 \times 10^{-4} cm^{-1}$) quite well. The ADF calculations did not reveal any unusually large superhyperfine couplings, neither with hydrogen (all between 0 and $6 \times 10^{-4} \, cm^{-1}$) nor with nitrogen nuclei (all between 1 and $20 \times 10^{-4} \, cm^{-1}$). However, they did reveal very large principle values of the iridium quadrupole tensor ($Q_1^{Ir}= -7 \times 10^{-4} \, cm^{-1}$, $Q_2^{Ir}= -21 \times 10^{-4} \, cm^{-1}$ and $Q_3^{Ir}= +28 \times 10^{-4} \, cm^{-1}$). In EPR powder simulations of spectra from quadrupolar first- and second row transition metals, the quadrupole interaction term $I \cdot Q \cdot I$ is usually neglected in the

spin hamiltonian, because it contributes only marginally to the spectral fine structure. However, in our case the DFT calculations indicate that the NQI could be comparable to the iridium HFI and therefore this approximation is no longer valid.

Recently, Rieger et al.,[2] who studied $[Tp'Ir(CO)(PPh_3)]^+$ (Tp' = hydrotris(3,5-dimethylpyrazolyl)borate) and other related paramagnetic iridium compounds required inclusion of the quadrupole term to simulate the EPR spectra of these compounds. In their case the "quadrupole effect" led to shifts of the allowed EPR transitions in the HFI multiplets causing a quartet to be converted into a 1:2:1 triplet. A similar effect seems to be present in our spectrum at the g_1 position. However, in addition we also observe two weak satellite lines.

The simulated spectrum in Figure 1 (see main text) was generated using the "best fit" spectral parameters listed in Table 1 (see main text). All interaction tensors are assumed to coincide (same principle axes). The values for A^N_1 and A^N_2 are not significant since no nitrogen HFI was observed along the g_1 and g_2 axis. Likewise A^{Ir}_2 is only an upper limit since no Ir HFI was observed along the g_2 axis. For the same reason the NQI "rhombicity parameter" η is not very accurate but should be regarded as an upper boundary. The simulation does show the additional satellites at the g_1 position. These lines turn out to be "forbidden" ($\Delta m_I = 2$) transitions and can be explained as follows:

The general spin hamiltonian for our system is formulated as:

$$H = \beta \mathbf{B} \cdot \mathbf{g} \cdot \mathbf{S} + \mathbf{S} \cdot \mathbf{A} \cdot \mathbf{I_{Ir}} + \mathbf{S} \cdot \mathbf{A} \cdot \mathbf{I_N} + \mathbf{I} \cdot \mathbf{P} \cdot \mathbf{I} \qquad (1)$$

The quadrupole term, when defined on principle axes, can also be written as:

$$\mathbf{I} \cdot \mathbf{P} \cdot \mathbf{I} = K\{(3I_z^2 - I^2) + \eta(I_x^2 - I_y^2)\} \qquad (2)$$

where $P_3 = 2K$, $P_1 = -K(1-\eta)$, $P_2 = -K(1+\eta)$.

Let us assume for simplicity that $\eta=0$ and that the nitrogen HFI can be neglected. With the magnetic field oriented along the g_3 axis, the spin hamiltonian can be written as:

$$H = g_3\beta B S_z + S_z A_3 I_z^{Ir} + K(3I_z^2 - I^2) \qquad (3)$$

The field dependent energy level diagram for this case can be readily calculated and is represented in Figure S1. It shows that the NQI shifts the $m_I=\pm3/2$ levels over the $m_I=\pm1/2$ levels in both m_S manifolds. Since the spin Hamiltonian (3) is defined in terms of z-operators (S_z and I_z), the m_I values are good quantum numbers and no forbidden transitions are observed. At the same time it is clear that the NQI shift is not affecting the spacing in the HFI multiplet at all. Therefore, the quadrupole effect is not visible at the g_3 position.
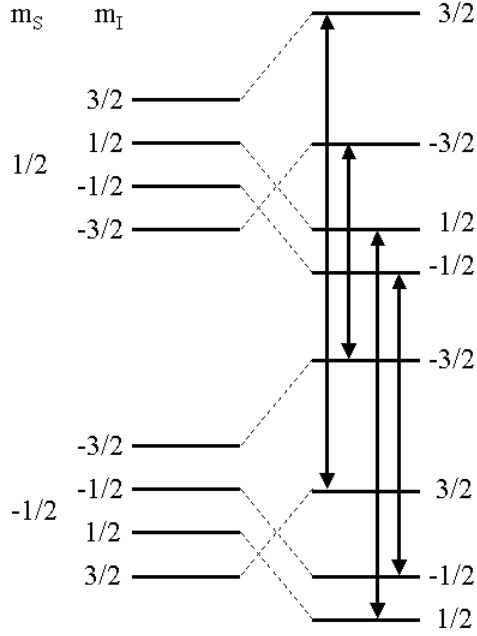
Figure S1. *Effect of first order contribution of NQI on energy levels and allowed EPR transitions in case B // z-axis. The Iridium HFI is assumed to be much larger than the Zeeman interaction.*

Now consider the situation when the magnetic field is oriented along g_1. In this case the spin Hamiltonian is written as:

$$H = g_1\beta B S_x + S_x A_1 I_x^{Ir} + K(3I_z^2 - I^2) \qquad (4a)$$

A permutation of the axis labels (x,y,z) enables to write the Hamiltonian in a more convenient form:

$$H = g_1\beta B S_z + S_z A_1 I_z^{Ir} + K(3I_x^2 - I^2) \qquad (4b)$$

Since the quadrupole term no longer commutes with the rest of the spin hamiltonian we need exact diagonalisation to obtain the energy levels and eigenfunctions.
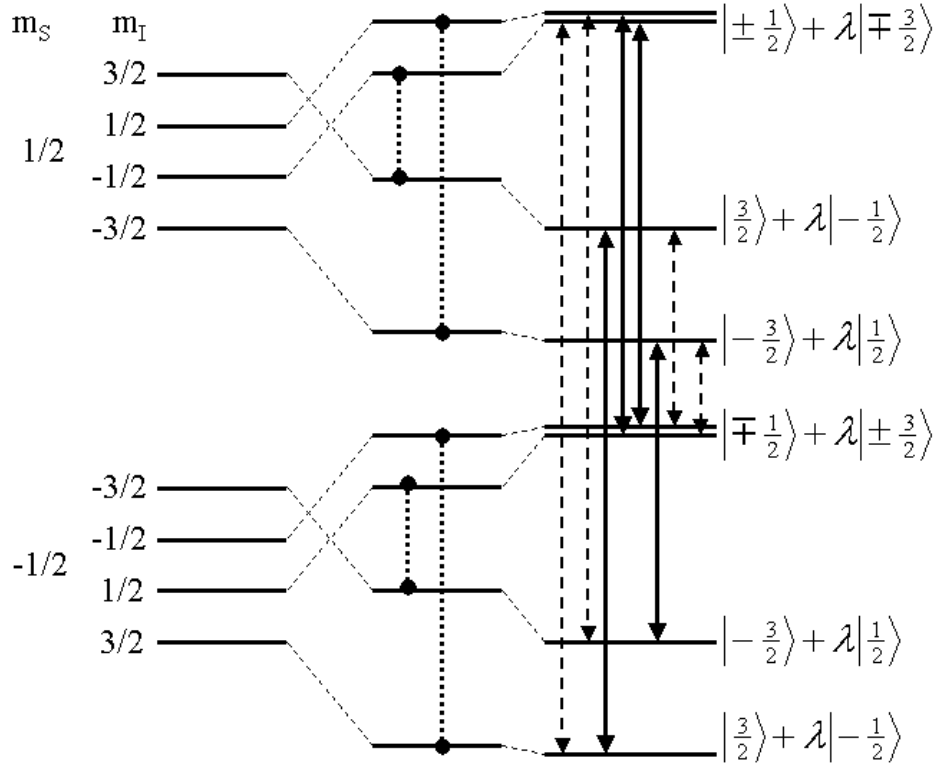
Figure S2. *Effect of first order and second order contribution of NQI on energy levels and EPR transitions for the case B//g₁-axis. The dotted lines indicate the mixing between $\left|\pm\frac{1}{2}\right\rangle$ and $\left|\mp\frac{3}{2}\right\rangle$ m_I spin functions caused by the I_x^2 operator in spin hamiltonian (4b). Because of this mixing forbidden trasitions occur which are indicated by the dashed arrows.*

The energy levels for this case are presented in Figure S2 together with a simplified representation of the spin eigenfunctions. The diagonal elements of the I_X^2 operator shift the $m_I=\pm1/2$ stronger than the $m_I=\pm3/2$ levels, this as opposed to the I_z^2 operator. Therefore, the total first order effect (including I^2) of the NQI on the nuclear spin levels for the g_1 case is the reverse of that for the g_3 case, i.e. the $m_I=\pm3/2$ levels are shifted downwards while the $m_I=\pm1/2$ levels are moved upwards. Since the I_X^2 operator only mixes $m_I = \pm(3/2\leftrightarrow-1/2)$ levels we expect only $\Delta m_I=2$ forbidden transition to occur along the g_1 axis. Due to the strong mixing the $m_I = \pm1/2$ as well as the $m_I = \pm3/2$ doublets are "pushed" towards each

other causing a general shrinking of the "allowed" HFI multiplet. In fact, in our case the $m_I = \pm 1/2$ doublets are coinciding leading to the 1:2:1 triplet for the allowed transitions. In addition two sets of "forbidden satellites" are generated one of which is almost coinciding with the outer transitions of the central triplet. This relatively complicated pattern of overlapping allowed and forbidden transitions leads to the pentet observed experimentally.

It is remarkable that the calculated principal value Q_3 of the Q-tensor from the ADF-DFT theory is quite close to the experimentally observed value (see Table 1). The rhombicity parameter ($\eta=0.5$) however has been clearly overestimated. A simulation with $\eta=0.5$ did not give the experimentally observed shape of the multiplet at g_1.

Details of the X-ray structure determinations

Relevant structure data are given in Tables S1 and S2. The structures were solved using the Patterson option[3] of the DIRDIF program system.[4] All nonhydrogen atoms were refined with anisotropic temperature factors. The hydrogen atoms were placed at calculated positions except for the hydrogen atoms attached to C1 of $5b^{2+}$, which were found from a difference fourier map, and refined isotropically in riding mode. For all structures in this report geometrical calculations[5] revealed neither unusual geometric features, nor unusual short intermolecular contacts. The calculations also revealed no higher symmetry and no (further) solvent accessible areas.

1^+: The EMPABS procedure[6] by itself was not adequate enough. The difference Fourier map showed peaks up to 3.6 Å^3 close to the Ir atom. Therefore an additional absorption correction was applied using the DIFABS procedure,[7] resulting in final residual peaks up to 2.3 Å^3. Based on geometrical considerations alone, the unit cell could be transformed to a orthorhombic C-cell (a = 9.1795(19), b = 46.2562(78), c = 11.5840(17) Å), but this transformation is not supported by the symmetry of the data (R(int) = 0.549) nor by the unit cell contents.

1^{2+}: From the anisotropic thermal displacement parameters for the PF_6 moieties it is clear that some atoms show a large positional disorder. Although it is possible to use several partially occupied positions for these atoms, no physically reasonable models result from these parameters, at least not any better than the models presented here.

3^{4+}: A few atoms, C53, C54 and C55, showed large disorder and were split into two partially occupied parts. Even then one of the two parts still shows large disorder, but further

splitting doesn't improve the physical model. The same holds for some of the fluorine atoms for which no other models could be found that would result in a stable refinement.

4b^{4+}: From the anisotropic thermal displacement parameters for the PF_6 and DMSO moieties it is clear that some atoms show a large positional disorder. Although it is possible to use several partially occupied positions for these atoms, no physically reasonable models result from these parameters, at least not any better than the models presented here. The assignment of atomic species in the DMSO moiety is based on bond distances and equivalent isotropic thermal displacement parameters.

6^{2+}: The cell dimensions show the characteristics of the orthorhombic crystal system but the intensity statistics, the symmetry of the crystal packing and the results of the crystal structure determination clearly indicate point group 2/m. The refinement procedure[8] clearly indicated that the weighting scheme should solely be based on Fo^2.

Table S1. Crystallographic data of complexes **1-3**.

	$[\mathbf{1}]^+(PF_6)$	$[\mathbf{1}]^{2+}(PF_6)_2$	$[\mathbf{2}]^+(PF_6)$	$[\mathbf{3}]^{4+}(PF_6)_4.MeCN$
Empirical formula	$C_{23}H_{28}F_6IrN_4P$	$C_{23}H_{28}F_{12}IrN_4P_2$	$C_{22}H_{26}F_6IrN_4P$	$C_{50}H_{61}F_{24}Ir_2N_{11}P_4$
Crystal color	Transparent brown-red	Black	Transparent red-brown	Transparent colorless
Crystal shape	Rounded lump	Rather regular fragment	Rather regular fragment	Regular rod
Crystal size [mm]	0.45 x 0.21 x 0.12	0.40 x 0.18 x 0.18	0.53 x 0.48 x 0.26	0.42 x 0.26 x 0.18
Molecular weight	697.66	842.63	683.64	1780.38
T [K]	293(2)	293(2)	293(2)	293(2)
Crystal system	Monoclinic	Monoclinic	Monoclinic	Triclinic
Space group	$P2_1/c$	$P2_1/c$	$P2_1/c$	$P-1$
Volume [Å^3]	2459.7(7)	2890.0(8)	2433.7(4)	3174.7(5)
a [Å]	9.1802(19)	13.072(2)	13.9423(10)	12.1371(10)
b [Å]	11.5828(18)	12.454(2)	13.2295(14)	14.9716(12)
c [Å]	23.581(4)	18.860(3)	14.7294(15)	19.096(2)
α [°]	90	90	90	73.115(8)
β [°]	101.193(19)	109.734(11)	116.392(10)	80.005(8)
γ [°]	90	90	90	73.965(8)
$\rho_{calcd.}$ [g·cm^{-3}]	1.884	1.937	1.866	1.862
Diffractometer	Enraf-Nonius CAD4	Enraf-Nonius CAD4	Enraf-Nonius CAD4	Enraf-Nonius CAD4
Abs. Cf. [mm^{-1}]	5.558	4.830	5.616	4.404
Radiation	Mo-$K\alpha$	Mo-$K\alpha$	Mo-$K\alpha$	Mo-$K\alpha$
Wavelength [Å]	0.71073	0.71073	0.71073	0.71073

Table S1. Crystallographic data of complexes **1-3**, continued

	$[1]^+(PF_6)$	$[1]^{2+}(PF_6)_2$	$[2]^+(PF_6)$	$[3]^{4+}(PF_6)_4.MeCN$
F(000)	1360	1636	1328	1736
Θ range [^{o}]	2.87 – 27.49	2.82 – 27.42	2.78 – 27.49	2.70 – 27.49
Index ranges	$0 \leq h \leq 11$	$-16 \leq h \leq 0$	$-18 \leq h \leq 0$	$-15 \leq h \leq 15$
	$-15 \leq k \leq 0$	$-16 \leq k \leq 0$	$-17 \leq k \leq 0$	$0 \leq k \leq 19$
	$-30 \leq l \leq 30$	$-23 \leq l \leq 24$	$-17 \leq l \leq 19$	$-23 \leq l \leq 24$
Abs. Corr.	Semi-empirical from ψ-scans	Semi-empirical from ψ-scans	Semi-empirical from ψ-scans	Semi-empirical from ψ-scans
Measured reflections	5961	6860	5783	15112
Unique reflections	5616	6569	5560	14554
[R_{int}]	0.0482	0.0199	0.0261	0.0204
Observed reflections [$I_0 > 2\sigma(I_0)$]	3815	5292	4362	11003
Data/ restrains /parameters	5616/ 0/ 319	6569/ 0/ 382	5560/ 0/ 309	14554/ 0/ 857
Goodness-of-fit on F^2	1.064	1.051	1.106	1.065
SHELXL-97 weight parameters	0.0553, 10.7359	0.0544, 8.4279	0.0646, 3.2862	0.0451, 6.2107
Final R_1, wR_2 [$I > 2\sigma(l)$]	0.0529, 0.1150	0.0393, 0.0939	0.0444, 0.1066	0.0379, 0.0882
R_1, wR_2 [all data]	0.0911, 0.1314	0.0546, 0.1011	0.0619, 0.1140	0.0587, 0.0966
Diff. Peak and hole [$e^.Å^{-3}$]	2.249, -2.322	1.589, -2.017	2.909, -1.382	1.162, -0.809

Table S2. Crystallographic data of complexes **4-6** and **8**.

	[4b]$^{4+}$(PF$_6$)$_4$. DMSO	[5b]$^{2+}$(PF$_6$)$_2$	[6]$^{2+}$(BPh$_4$)$_2$. MeOH	[8]$^{2+}$(BPh$_4$)$_2$. MeOH
Empirical formula	C$_{25}$H$_{33}$F$_{12}$IrOP$_2$S	C$_{21}$H$_{24}$ClF$_6$IrN$_4$P	C$_{72}$H$_{70}$B$_2$IrN$_5$O$_2$	C$_{81}$H$_{91}$B$_2$IrN$_6$O$_3$
Crystal color	Transparent colorless	Transparent light yellow	Dark yellow/brown	Transparent yellow
Crystal shape	Regular rod	Rough fragment	Rough fragment	Rough fragment
Crystal size [mm]	0.50 x 0.18 x 0.11	0.18 x 0.14 x 0.12	0.17 x 0.15 x 0.14	0.22 x 0.18 x 0.14
Molecular weight	933.76	705.06	1251.15	1410.42
T [K]	293(2)	150(2)	208(2)	208(2)
Crystal system	Triclinic	Monoclinic	Monoclinic	Triclinic
Space group	P –1	P2$_1$/n	P2$_1$/c	P –1
Volume [Å^3]	1709.0(9)	2317.05(8)	6100.7(9)	3478.1(6)
a [Å]	12.500(2)	10.5432(2)	17.6536(18)	14.4595(18)
b [Å]	12.837(4)	16.3409(3)	12.4640(10)	15.1210(15)
c [Å]	13.093(5)	13.4964(3)	27.7263(17)	19.5755(8)
α [^{o}]	61.49(3)	90	90	86.599(9)
β [^{o}]	75.105(19)	94.8074(9)	90.002(7)	68.876(5)
γ [^{o}]	68.503(18)	90	90	61.576(9)
ρ$_{calcd.}$ [g·cm^{-3}]	1.815	2.021	1.362	1.347
Diffractometer	Enraf-Nonius CAD4	Enraf-Nonius CAD4	Nonius-Kappa CCD	Nonius-Kappa CCD
Abs. Coef. [mm^{-1}]	4.155	6.013	2.239	1.973
Radiation	Mo-$K\alpha$	Mo-$K\alpha$	Mo-$K\alpha$	Mo-$K\alpha$
Wavelength [Å]	0.71073	0.71073	0.71073	0.71073

Table S2. Crystallographic data of complexes **4-6** and **8**, continued.

|	[**4b**]$^{4+}$(PF$_6$)$_4$. DMSO	[**5b**]$^{2+}$(PF$_6$)$_2$	[**6**]$^{2+}$(BPh$_4$)$_2$. MeOH	[**8**]$^{2+}$(BPh$_4$)$_2$. MeOH
F(000)	914	1364	2560	1460
Θ range [^{o}]	2.93 – 27.47	1.960 – 27.400	3.16 - 27.50	3.52 – 27.50
Index ranges	-16 ≤ h ≤ 0	-13 ≤ h ≤ 13	-22 ≤ h ≤ 22	-18 ≤ h ≤ 18
	-16 ≤ k ≤ 15	-21 ≤ k ≤ 20	-16 ≤ k ≤ 15	-19 ≤ k ≤ 19
	-16 ≤ l ≤ 16	-17 ≤ l ≤ 17	-36 ≤ l ≤ 36	-25 ≤ l ≤ 25
Abs. Corr.	Semi-empirical from ψ-scans	Multiscan Procedure	SADABS multiscan correction[9]	SADABS multiscan correction[9]
Measured reflections	8189	41246	65334	126903
Unique reflections	7831	5253	13606	15942
[R$_{int}$]	0.0149	0.0913	0.0714	0.0391
Observed reflections [I$_0$>2σ(I$_0$)]	6621	3981	7072	14183
Data/ restrains /parameters	7831/ 0/ 430	5253/ 0/ 315	13606 / 0 / 744	15942/ 0 /849
Goodness-of-fit on F^2	1.093	1.023	0.656	1.113
SHELXL-97 weight parameters	0.0678, 0.9425	0.0192, 1.1943	0.0000, 0.0000	0.0133, 3.2045
Final R_1, wR$_2$ [I> 2σ(l)]	0.0408, 0.1032	0.0285, 0.0528	0.0446, 0.1221	0.0248, 0.0487
R_1, wR$_2$ [all data]	0.0538, 0.1101	0.0536, 0.0582	0.1084, 0.1756	0.0341, 0.0516
Diff. Peak and hole [e$^-$Å^{-3}]	1.159, -0.914	1.832, -1.015	1.367, -0.432	0.899, -0.912
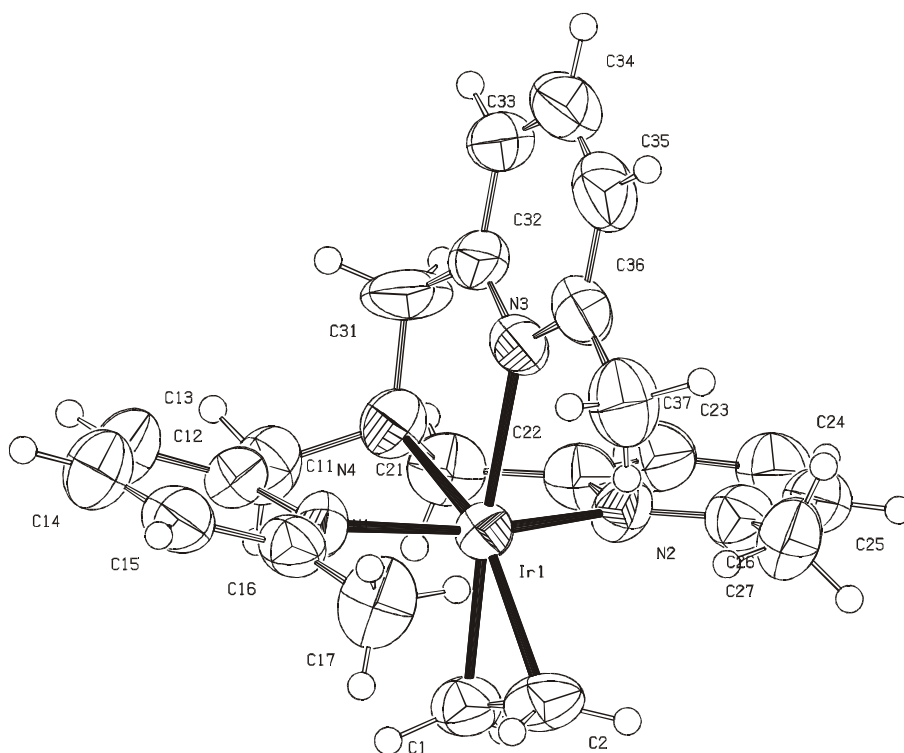
Figure S3. ORTEP drawing of complex **1**$^+$ (drawn at 50% probability level).
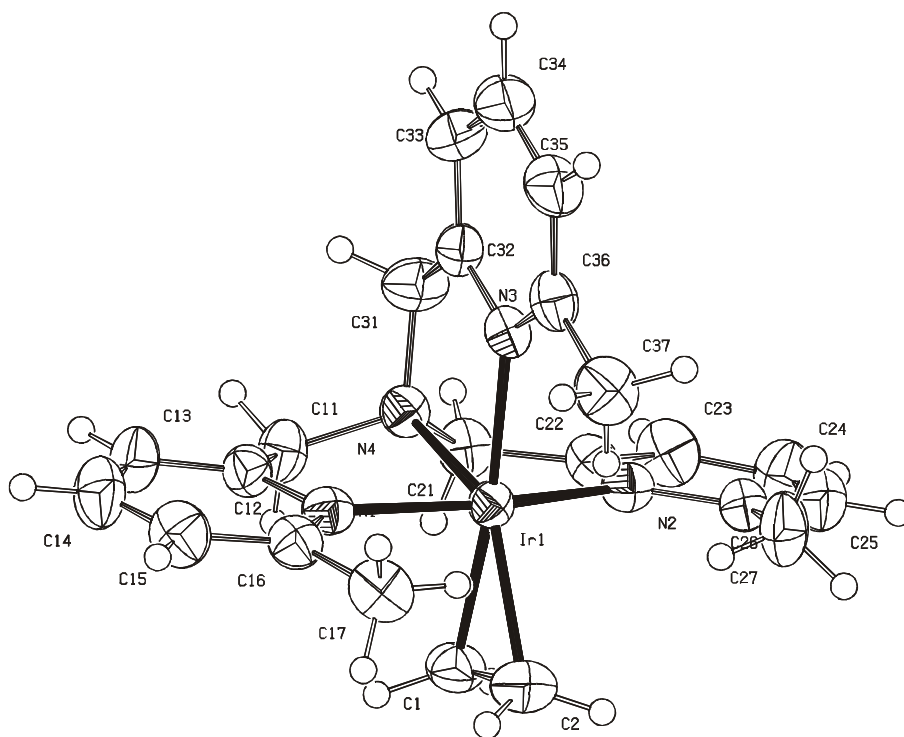

Figure S4. ORTEP drawing of complex **1**$^{2+}$ (drawn at 50% probability level).
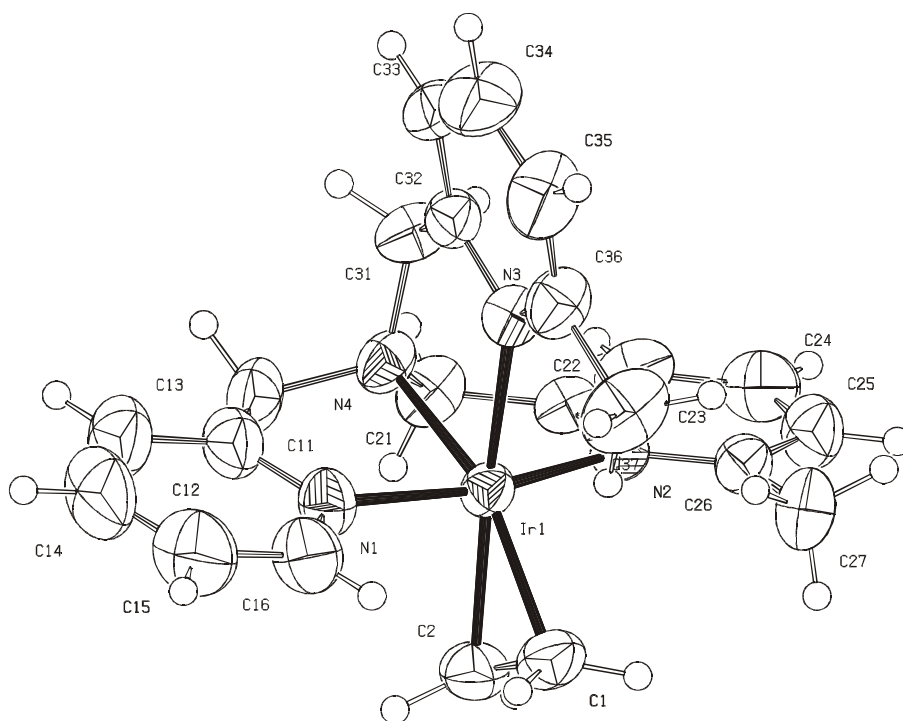
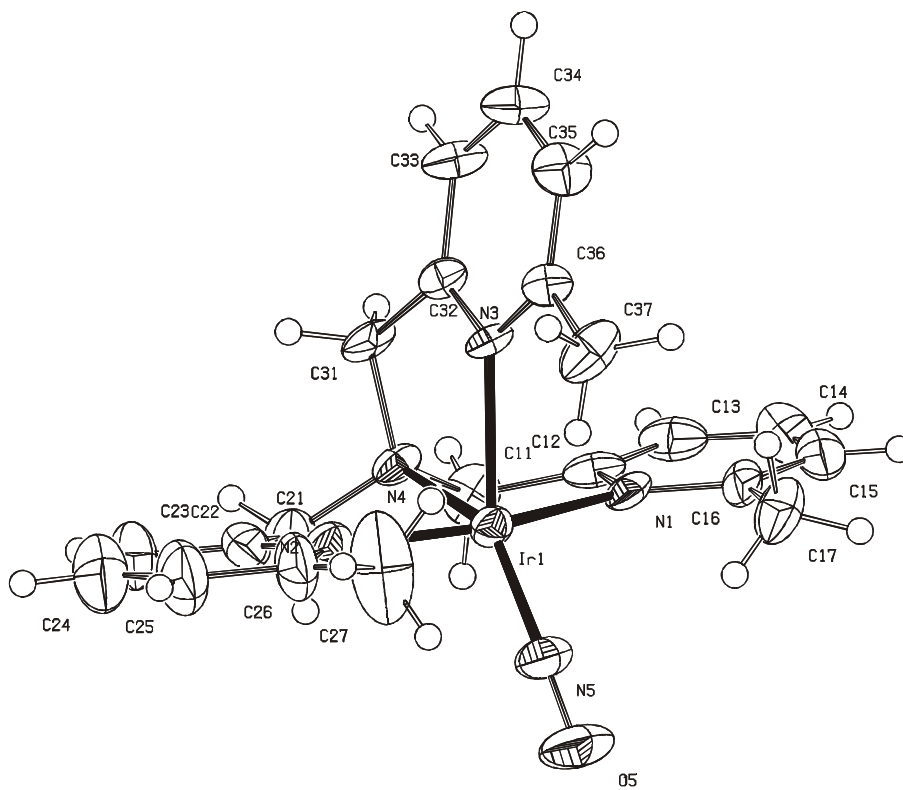**Figure S5**. ORTEP drawing of complex **2**$^+$ (drawn at 50% probability level).

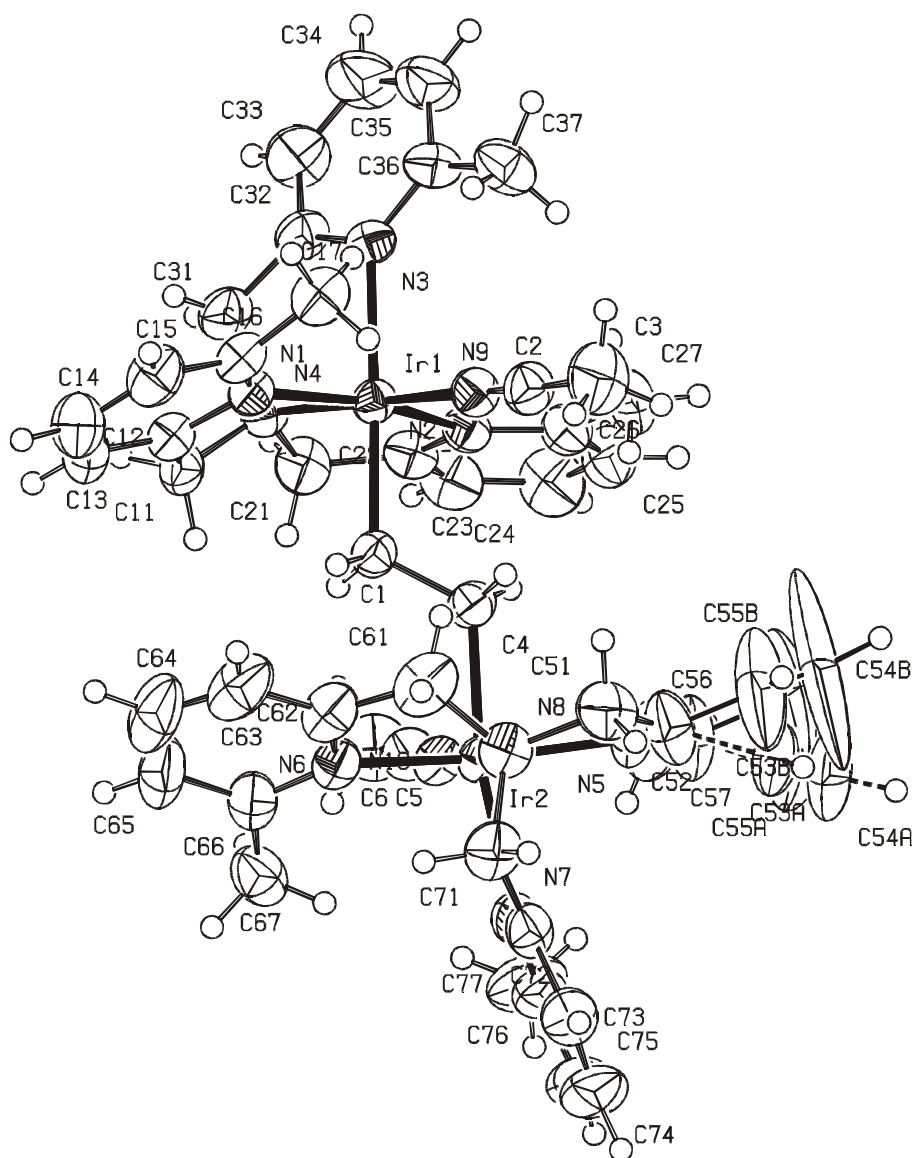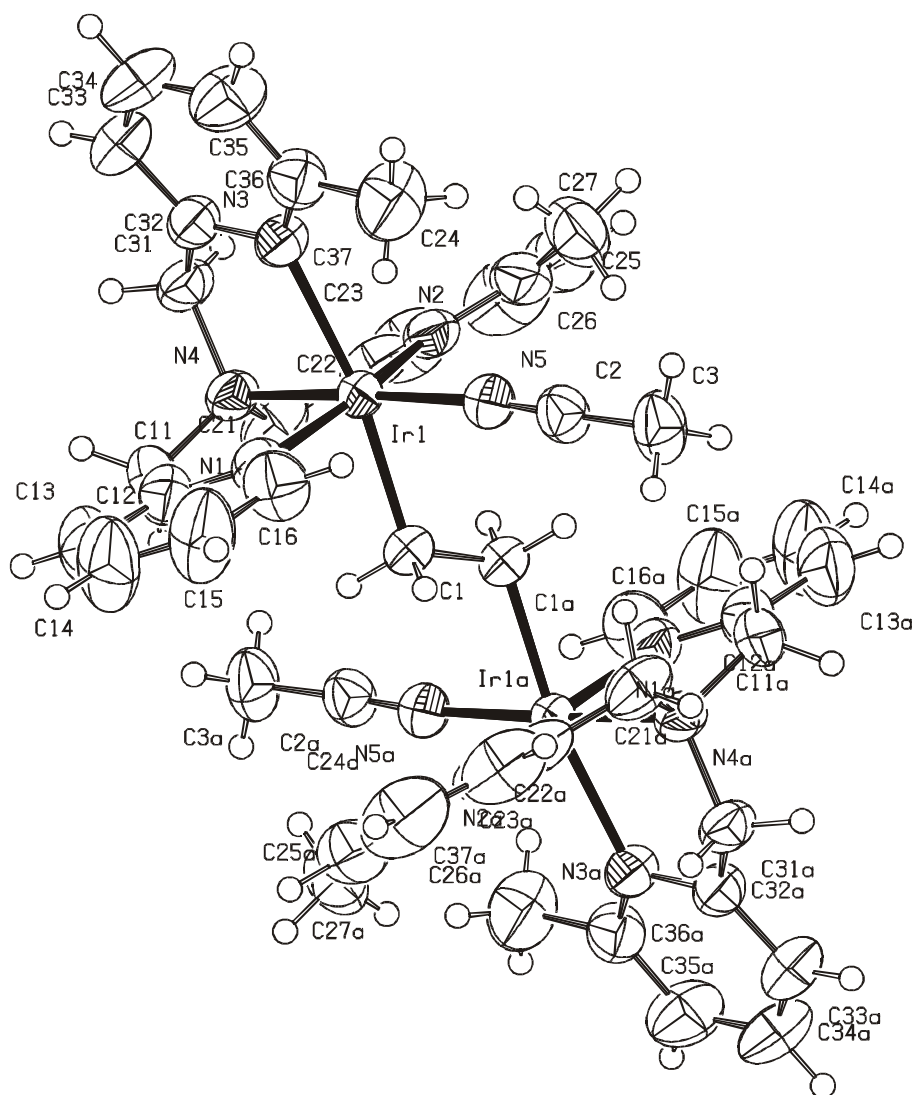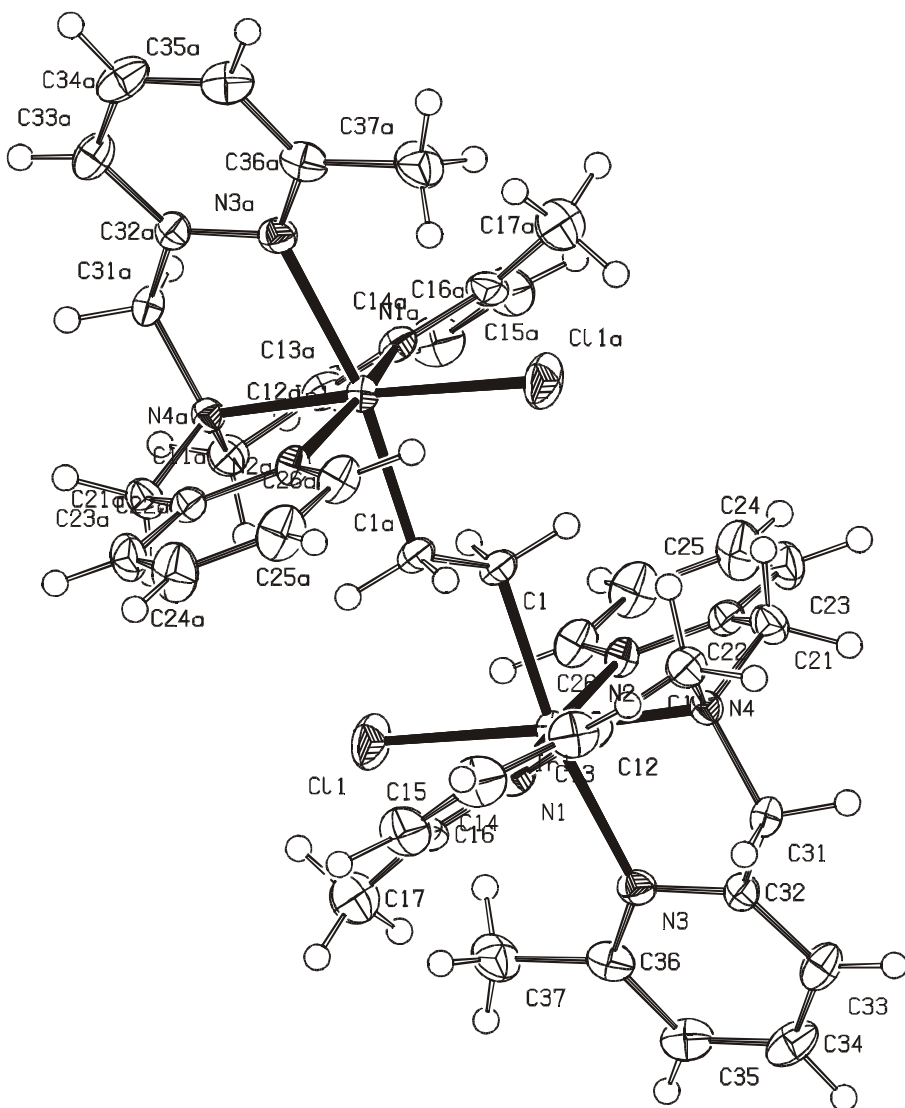**Figure S6**. ORTEP drawing of complex **6**$^{2+}$ (drawn at 50% probability level).

Figure S7. ORTEP drawing of complex $\mathbf{3}^{4+}$ (drawn at 50% probability level).

Figure S8. ORTEP drawing of complex **4b**[4+] (drawn at 50% probability level).

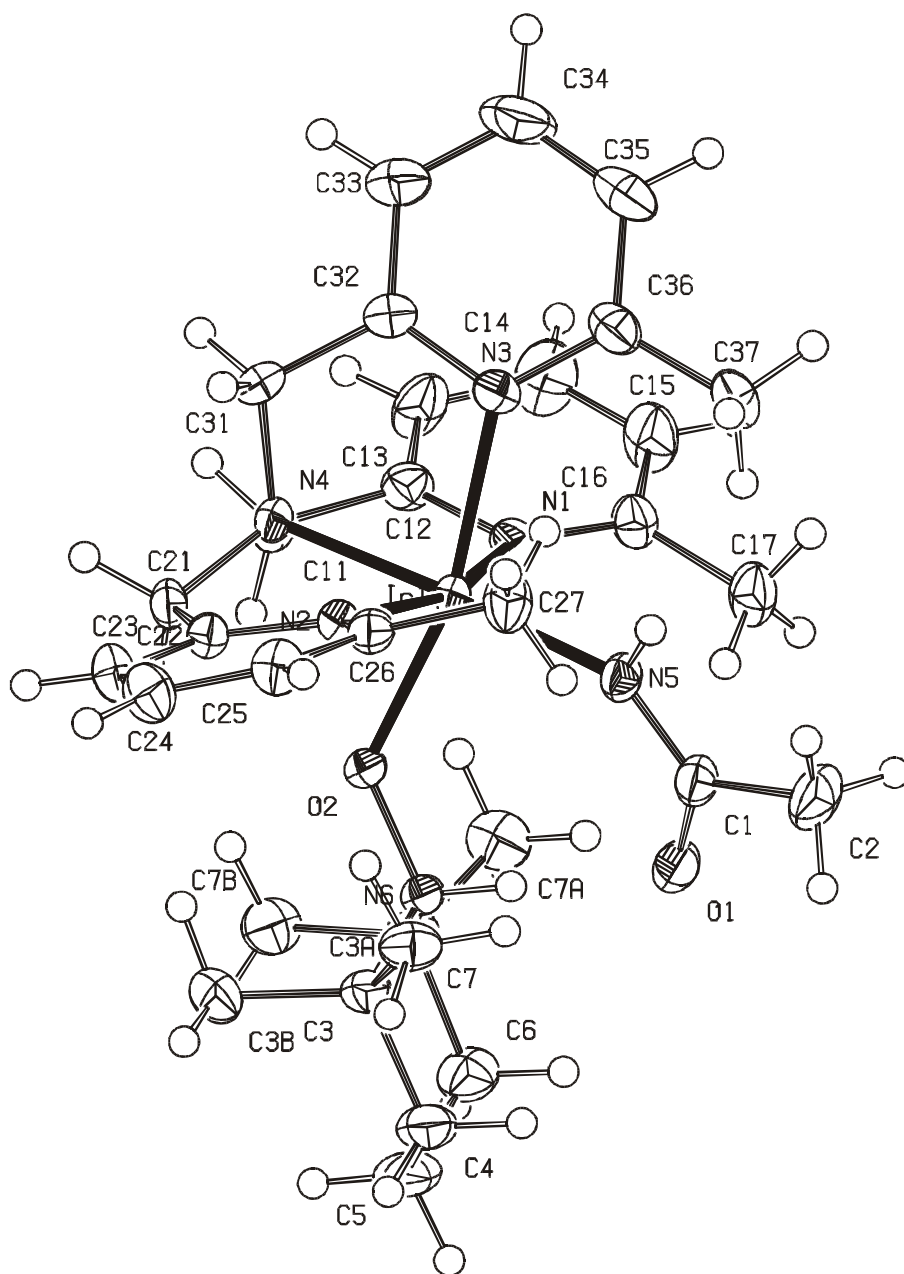**Figure S9**. ORTEP drawing of complex **5b**[2+] (drawn at 50% probability level).

Figure S10. ORTEP drawing of complex **8**$^{2+}$ (drawn at 50% probability level).

References

1) de Bruin, B.; Peters, T.P.J.; Thewissen, S.; Blok, A.N.J.; Wilting, J.B.M.; de Gelder, R.; Smits, J.M.M.; Gal, A.W.; Angew. Chem. Int. Ed., 2002, 41 (12), 2135-2138.

2) Connely, N.G.; Emslie, D.J.H.; Klangsinsirikul, P.; Rieger, P.H., J. Phys. Chem. A., 2002, 106, 12214.

3) Beurskens, P.T.; Beurskens, G.; Strumpel, M.; Nordman, C.E., in *Patterson and Pattersons*, Clarendon, Oxford, **1987**, p.356.

4) Beurskens, P.T.; Beurskens, G.; Bosman, W.P.; de Gelder, R.; García-Granda, S.; Gould, R.O. Israël, R.; Smits, J.M.M., University of Nijmegen, The Netherlands, **1996**.

5) Spek, A.L., University of Utrecht, The Netherlands, **1995**.

6) North, A.C.T.; Philips, D.C.; Mathews, F.S. *Acta Crystallogr.* **1968**, *A24*, 351.

7) Walker, N; Stuart, D. *Acta Crystallogr.* **1983**, *A39*, 158.

8) Sheldrick, G.M. SHELXL-97. Program for the refinement of crystal structures; University of Göttingen: Germany, **1997**.

9) Sheldrick, G.M. SADABS. Program for Empirical Absorption Correction; University of Göttingen: Germany, **1996.**